

Discrete element method approach to simulate the thermo-mechanical behaviour of thermal barrier coatings during a thermal cycle

Ilyes Bensemmane^{1,2*}, Willy Leclerc¹, Nabil Ferguen³, Mohamed Guessasma¹, and Mohamed El-Amine Djeghlal²

¹ Laboratoire des Technologies Innovantes (LTI) Université de Picardie Jules Verne, Saint Quentin, France

² Laboratoire Science et Génie des Matériaux (LSGM) Ecole Nationale Polytechnique, Algérie

³ Centre de Développement des Technologies Avancées (CDTA), Algérie

Abstract: Thermal Barrier Coatings (TBCs) are advanced multilayer structures designed to provide thermal insulation for Ni-based superalloy components used in gas turbine blades. These coatings enhance the performance of the components by enabling them to withstand higher temperatures ($\sim 1100^\circ\text{C}$). However, the complex microstructure of TBCs, combined with harsh operational environments, generate thermal and mechanical stresses and eventually lead to failure. Key failure mechanisms include creep deformation due to prolonged high-temperature exposure and thermal stresses arising from Coefficients of Thermal Expansion (CTE) mismatch. In this study, we propose a numerical model based on the Discrete Element Method (DEM) to investigate the development of thermal residual stresses within TBCs during the thermal cycle considering creep and CTE mismatch effects. A DEM viscoelastic creep model based on Norton's law is first validated in the context of tensile and shear tests by comparison with the Finite Element Method (FEM) and the theory. In a second step, the proposed DEM approach is applied to the case of a multi-layer model of TBC microstructure derived from a real SEM image. Numerical simulations are led in the context of a thermal cycling including thermal expansion and creep effects as well as the growth of an oxide layer at high temperature. Results highlight that the DEM model accurately simulate the creep deformation and predicts thermal stresses that contribute to the failure of TBC systems under thermal loading.

Keywords: Thermal barrier coatings, Discrete Element Method, Creep behavior, Coefficients of thermal expansion mismatch

Introduction

TBCs are multilayered systems designed to protect turbine blades in gas turbines and aeroengines which are exposed to extreme temperatures particularly at the turbine entry gas that may exceed 1100°C . TBCs consist of a ceramic top coat (TC), typically made from Ytria-Stabilized Zirconia (YSZ) due to its excellent thermal insulation properties, an intermetallic Bond Coat (BC), and a Thermally Grown Oxide (TGO) layer that forms between the TC and BC at high temperatures (Figure 1). TBCs significantly enhance turbine performance by reducing surface temperatures up to 300°C (Feuerstein et al. (2008)).

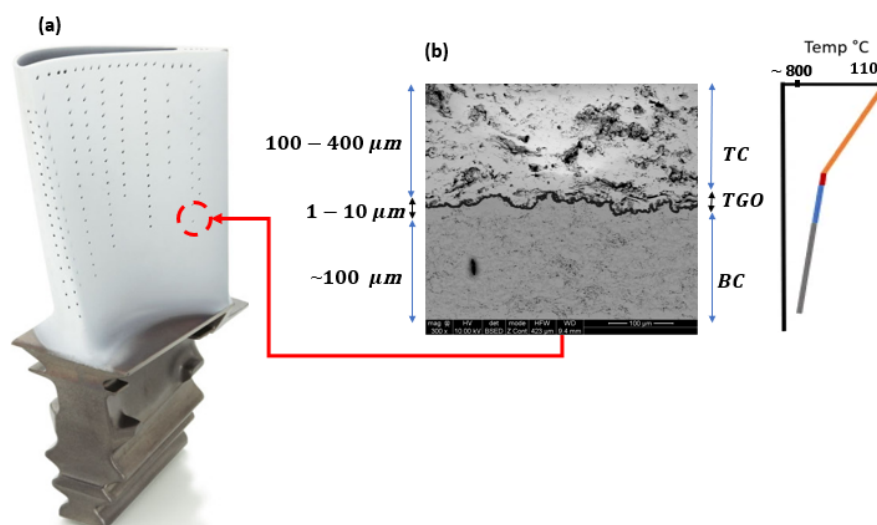


Fig. 1: (a) Coated turbine blade (b) SEM cross-section of TBC system obtained by plasma spraying process and related operating temperatures

Despite their effectiveness, TBCs have a complex microstructure due to their defects and multilayer nature, which raises a number of issues in predicting their lifetime and detecting early failure at high-temperatures. Failure mechanisms in TBCs are often

associated with residual stresses resulting from the CTE mismatch between layers, the thickness and roughness of the TGO layer, and stress redistribution due to high-temperature creep. These contribute to residual stresses, which cause cracks to form. TBC failure typically involves delamination at the BC/TGO interface and crack formation in the TC layer. The roughness and instability of the TGO layer play a crucial role by causing stress that drives both delamination and crack propagation. Failure initiation and propagation in TBCs occur through various mechanisms as seen in Figure 2, BC/TGO delamination (mechanism I) happens during cooling phase and moves through the TGO layer. TGO/TC delamination (mechanism II) occurs due to the TGO layer formation beneath the TC layer. The merging of these cracks (mechanism IV) can lead to the TBC system spallation, as the TGO thickens, the CTE of the BC/TGO becomes lower than that of both the TC and the BC, which reverses the nature of the stresses in the TC undulation valley from compression to tension crack propagation within the TC (Rabiei and Evans (2000); Padture et al. (2002)). Additionally, crack propagation in the TC (mechanism III) layer is influenced by its microstructure and the brittle nature of the material (Padture et al. (2002)), which is determined by the deposition method, like Atmospheric Plasma Spray (APS) that results in a complex, layered structure with interconnected pores (Feuerstein et al. (2008)). Numerical studies based on the FEM have been extensively conducted to analyze stress distribution and failure mechanisms in TBCs. For instance, Aktaa et al. (2005) developed a method to model cracks in critical areas of the TBC. They used a modified technique to study how cracks close and added a way to predict how cracks would spread based on mixed failure modes. Ranjbar-Far et al. (2010) used a 2D unit cell model with a sinusoidal profile to investigate TBC failure mechanisms, highlighting the effect of the lamellar microstructure of the TC on stress distribution. Their findings showed that crack evolution is influenced by the growth of the oxide layer and interface roughness. Bäker (2012) examined the impact of asperity peak and valley regions at the TGO/TC interface on interfacial crack propagation. Kyaw et al. (2016) took advantage of a method for predicting the failure of a TBC system based on the combination of the eXtended Finite Element Method (XFEM) and Cohesive Zone Model (CZM) to respectively simulate cracks within bulk coatings and reproduce interfacial cracks. Cen et al. (2019) explored stress distribution and failure under thermal cycling conditions, considering TGO layer growth, thermal expansion, and creep effects. Originally, DEM was developed by Cundall (1974) for rock mechanics, and then used to model discrete systems that are challenging for continuous methods like FEM, as the granular flow and tribological triplet (Haddad et al. (2016); Ji et al. (2019)). Since then, it has been extended to simulate the thermo-mechanical behavior of continuous elastic media but also effectively modeling complex crack propagation (André et al. (2012); Leclerc et al. (2017)). Potyondy and Cundall (2004) developed the Bonded Particle Model (BPM) to simulate rock materials using bonded spherical particles. André et al. (2012) proposed a hybrid lattice-particle model which has been applied to study mechanical and thermo-mechanical behaviors of conventional and composite materials. André et al. (2013) also developed a method called Removed Discrete Element Failure (RDEF) that involves removing particles from a system when a failure criterion is met, this method leads to more realistic crack patterns and propagation in both homogeneous and heterogeneous materials. Additionally, a discrete CZM has been proposed and used to simulate delamination and fiber/matrix debonding in glass-fiber composite materials (Ammar et al. (2021)). In the context of TBCs, there are few studies dedicated to investigate failure mechanisms based on DEM modeling. Nevertheless, we can cite the recent works led by Leclerc et al. (2022) and Ferguen et al. (2023) which focus on interfacial debonding and crack propagation during a cooling phase. The DEM-based approach allows the complex microstructure to be modeled using SEM images of real microstructures, incorporating the TGO layer shape and temperature-dependent properties during cooling phases. In this paper, we extend the DEM-based 2D approach of Leclerc et al. (2022) to investigate the effects of creep on residual stresses during the thermal cycling of TBCs.

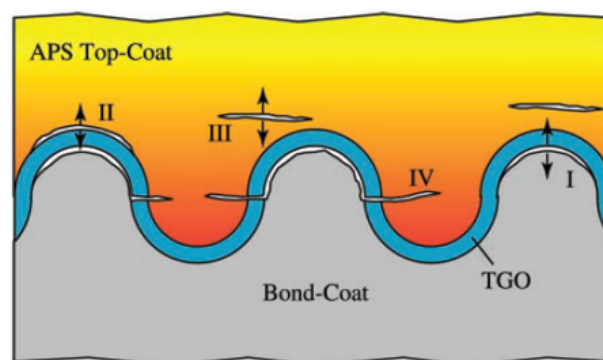


Fig. 2: Schematic diagram illustrating the four primary cracking mechanisms in APS TBCs (Padture et al. (2002))

1 DEM modeling

1.1 Hybrid lattice particulate model

In this study, we describe the hybrid lattice particulate model (André et al. (2012); Haddad et al. (2015); Leclerc et al. (2017)), employed to simulate the thermo-mechanical behavior of a continuous medium using DEM (André et al. (2012); Haddad et al. (2015)). Such an approach benefits from random particulate systems (generally composed of packed disks in 2D or spheres in 3D) connected by cohesive Euler-Bernoulli beam elements (Haddad et al. (2015); Leclerc (2017)), as depicted in Figure 3.

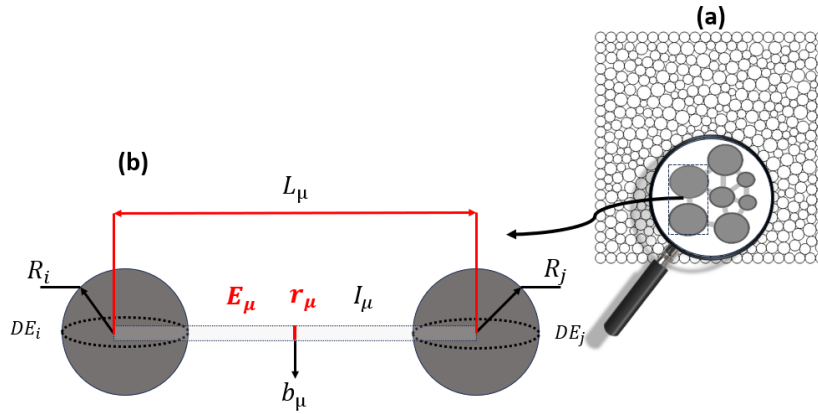


Fig. 3: (a) Particulate system with (b) zoom describing the cohesive beam model

In this study, we consider a 2D generation process that allows precise control over the intrinsic characteristics of the random particulate system (Haddad et al. (2015)). This controlled generation adjusts the overall mechanical properties of the continuous medium associated with the particulate system meets the requirements of "random closed packing" (RCP) (Torquato et al. (2000)), featuring a cardinal number of 4.6 and a volume fraction of 85% in the case of a 2D particulate system. To ensure isotropy and prevent directional effects, a slight variation in particle size, defined by a coefficient of 0.3, is incorporated (Haddad et al. (2015)). Each binary link in the contact network of the particulate system is replaced by a cohesive beam element. The generalized force vector associated with each Euler-Bernoulli beam element is determined by parameters such as beam length (L_μ), cross-sectional area (A_μ), quadratic moment (I_μ), and microscopic Young's modulus (E_μ) (Leclerc et al. (2017)). However, for sufficiently dense random particulate systems, the characterization primarily depends on two parameters: E_μ and the dimensionless beam thickness r_μ , which is directly linked to L_μ , A_μ , and I_μ . It is worth noting that acceleration, velocity, and particle position are determined according to Newton's second law of motion using explicit time integration. In addition, the velocity-Verlet scheme is considered to accurately compute the positions and velocities of a large set of particles throughout the simulation.

1.2 Mechanical behavior modeling

Initially, the relation between the microscopic parameters E_μ and r_μ and the macroscopic properties such as Young's modulus E_M and Poisson's ratio ν_M is a priori unknown. Therefore, a specific calibration process is employed to connect the microscopic and macroscopic coefficients of the continuum medium (Haddad et al. (2015)). This calibration employs polynomial functions P and Q , as demonstrated in the equations below:

$$r_\mu = P(\nu_M) \quad (1)$$

$$E_\mu = Q(r_\mu)E_M \quad (2)$$

The calibration process first involves deriving r_μ from ν_M , then determining E_μ based on r_μ and E_M . It should be noted that, under RCP assumptions, the functions P and Q were preliminary determined using specific tensile test (Haddad et al. (2015); Leclerc (2017)). To simulate failure mechanisms during a cooling phase, Leclerc et al. (2022) developed a discrete model of TBC comprising BC, TGO, and TC layers. Each layer was considered homogeneous and isotropic with its own temperature-dependent elastic properties. Based on the work of Cen et al. (2019), Leclerc et al. (2022) identified specific microscopic parameters corresponding to macroscopic elastic properties and coefficients of thermal expansion for each TBC layer mentioned in Table 1.

Tab. 1: Temperature-dependent data for coefficients of thermal expansion, Young's moduli, and Poisson's ratios of all layers (Ranjbar-Far et al. (2010); Leclerc et al. (2022))

T (°C)	Top-Coat			TGO			Bond-coat		
	$\alpha \times 10^{-6} \text{ } ^\circ\text{C}^{-1}$	E_M/E_μ (GPa)	ν_M/r_μ	$\alpha \times 10^{-6} \text{ } ^\circ\text{C}^{-1}$	E_M/E_μ (GPa)	ν_M/r_μ	$\alpha \times 10^{-6} \text{ } ^\circ\text{C}^{-1}$	E_M/E_μ (GPa)	ν_M/r_μ
25	9.68	17.5/29.8	0.2/0.63	5.1	380/1060.2	0.27/0.45	-	183/10.6	0.3/0.45
100	-	-	0.2/0.63	-	-	0.27/0.45	10.34	-	0.3/0.45
200	9.7	-	0.2/0.63	-	-	0.27/0.45	11.3	-	0.3/0.45
400	-	-	0.2/0.63	-	-	0.27/0.45	12.5	152/424.1	0.3/0.45
600	-	-	0.2/0.63	-	353/984.9	0.27/0.45	-	-	0.3/0.45
700	9.88	-	0.2/0.63	-	-	0.27/0.45	-	-	0.3/0.45
800	-	-	0.2/0.63	-	338/943	0.27/0.45	14.3	109/304.1	0.3/0.45
900	-	12.4/21.1	0.2/0.63	-	-	0.27/0.45	16	-	0.3/0.45
1000	10.34	-	0.2/0.63	9.8	312/870.5	0.27/0.45	-	-	0.3/0.45

1.3 Thermal expansion model

Throughout the simulation, a uniform temperature is imposed on the entire particulate system at each time step consisting of a gradual and linear heating phase from 25°C to 1100°C, followed by a cooling phase from 1100°C back to 25°C, both occurring

over a total duration of 300 seconds with a dwelling time of 10 hours between them. Additionally, each layer of the TBC responds differently during the three steps of the thermal cycle with respective temperature-dependent CTEs and creep parameters (Cen et al. (2019)). To account for thermal expansion effects, the initial length of the cohesive beam elements L_μ is adjusted according to the CTE (Figure 4) of each layer and the applied temperature T according to the model discussed by Alhaji-Hassan et al. (2020) as follows:

$$L_\mu = L_\mu(T_0)(1 + \alpha(T - T_0)) \quad (3)$$

with α that denotes the CTE of the corresponding layer. Thermal expansion is considered at the scale of the cohesive bond by adjusting its length based on temperature. The main idea is that the initial length of the cohesive bond (L_0) expands when the temperature increases (Figure 4) and contracts when the temperature decreases.

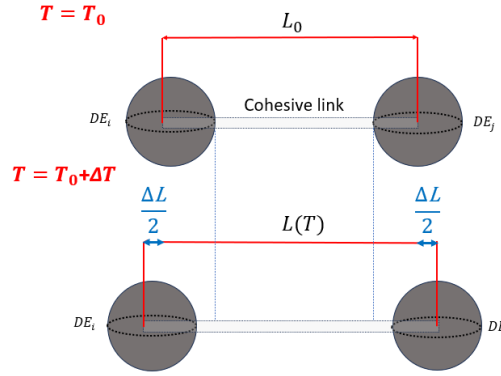


Fig. 4: Thermal expansion model at the cohesive link scale

1.4 Stress field determination

To account for thermal stresses in TBCs, Zhou's formulation (Zhou (2003)) is used to examine the stress field by linking the equivalent stress tensor to inter-particle contact forces and branch vectors between contacting particles as follows:

$$\overline{\overline{\sigma}}_i = \frac{1}{2\Omega_i} \sum_{j=1}^{Z_i} \frac{1}{2} (f_{ij} \otimes d_{ij} + f_{ji} \otimes d_{ji}) \quad (4)$$

where f_{ij} is the cohesion force vector applied to the particle i by a particle j , d_{ij} is the relative position vector between particles i and j and Z_i is the number of contacts between the particle i and its neighboring particles, Ω_i is the area of representation of the particle i which is approximated by the following expression:

$$\Omega_i = \frac{A_i}{\phi} \quad (5)$$

where A_i is the real area of the particle and ϕ is the volume fraction of the granular system which is 0.85 in the present work where granular packings meet the assumptions of an RCP. The symmetry of the stress tensor is ensured as described in equation (4). Note that without this symmetry, σ_i can not be symmetrical because the beam elements are not evenly distributed around each DE.

2 Viscoelastic creep model

2.1 Deviatoric Norton's law

Our primary objective is to incorporate the creep behavior to simulate the thermomechanical response of TBCs during the thermal cycle. Creep behavior refers to the gradual deformation of materials due to their long-term exposure to high temperatures under constant load. At high-temperature environment where TBCs operate (around 1100 °C), the rate of creep is significant and increases as the temperature rises, as described by the Arrhenius-type equation governing high-temperature processes. This study leverages Norton's law to predict time-dependent deformation during the stationary (secondary) creep stage (Hyde et al. (2014)), which in its tensorial form is:

$$\overline{\overline{\varepsilon}}_c = B \overline{\overline{\sigma}}_e^n \overline{\overline{n}}^D \quad (6)$$

With $\overline{\overline{\varepsilon}}_c$ is the strain rate tensor, B is a constant depending on the material and n is the creep power law exponent listed in Table 4, $\overline{\overline{\sigma}}_e$ is the equivalent Von-Mises stress and $\overline{\overline{n}}^D$ is the deviatoric tensor defined as :

$$\overline{\overline{n}}^D = 2 \frac{dev(\overline{\overline{\sigma}})}{\overline{\overline{\sigma}}_e} \quad (7)$$

In this work, creep-induced strain is incorporated similarly to thermal expansion by adjusting cohesive element lengths. This approach assigns the contributions of creep deformation to each beam element, as illustrated in Figure 5. The equation expressing the creep displacement added to each beam is as follows :

$$\begin{cases} U_x^c = \varepsilon_{xx}^c L_x + \varepsilon_{xy}^c L_y \\ U_y^c = \varepsilon_{yy}^c L_y + \varepsilon_{xy}^c L_x \end{cases} \quad (8)$$

where U_x^c, U_y^c are the total creep displacement according to x and y respectively, $\varepsilon_{xx}^c, \varepsilon_{yy}^c$ are the uniaxial creep strain according to x and y and ε_{xy}^c is the shear creep strain

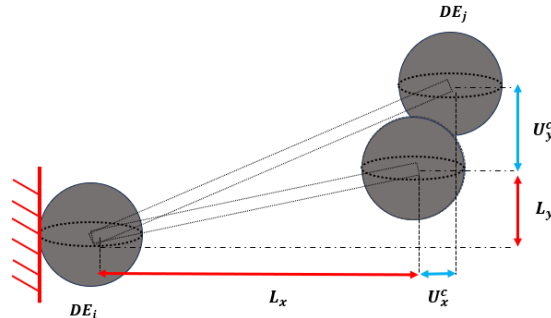


Fig. 5: Creep model incorporation at the cohesive link scale

2.2 Validation test

2.2.1 Tensile test

Tensile tests are performed under various loads to evaluate the implementation of the DEM creep model in comparison with FEM and analytical models. A 2D configuration of the particulate system is considered, as illustrated in Figure 6, it consists of a rectangular system with 1000 discrete elements (DE) generated according to Haddad et al. (2015) criterion and respecting the hypotheses of the RCP. The size of the domain measures 10^{-5} m in length (L) and $6.67 \cdot 10^{-5}$ m in width (b), subjected to a tensile load that is applied on the right side surface. Symmetry boundary conditions are applied to the left side surface to ensure a uniform stress field. The tensile test is conducted at a constant temperature of 1100°C on a homogeneous BC material during 10 hours of thermal exposure.

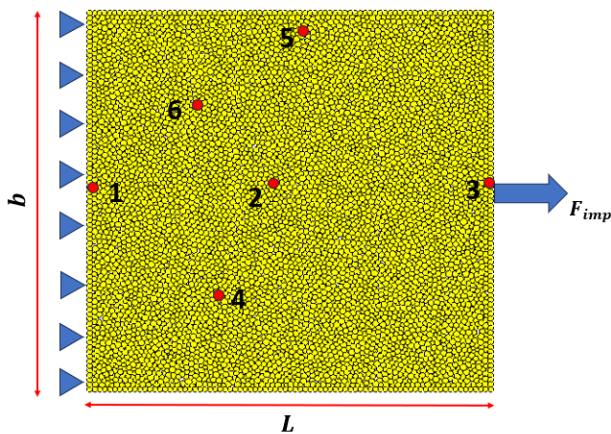


Fig. 6: Tensile test configuration and applied boundary conditions

Discrete element (DEs)	Coordinates (x,y)
1	(0L, 0.5b)
2	(0.5L, 0.5b)
3	(L, 0.5b)
4	(0.4L, 0.2b)
5	(0.6L, 0.8b)
6	(0.2L, 0.7b)

Tab. 2: Coordinates of DE 1 to 6

To ensure and validate the accuracy of the DEM-based model, creep displacements in the x and y directions are compared with theoretical and FEM estimates under three different load types: constant ($F_{imp} = 1.8 \cdot 10^{-2}$ N), linear ($F_{imp} = \frac{3.5 \cdot 10^{-2} t}{T}$ N), and cyclic ($F_{imp} = 1.6 \cdot 10^{-1} \sin(\frac{2\pi t}{T})$ N). The load intensities were chosen to ensure a maximum creep strain of 2%, where t is the creep time and T is the total time, set to 10 hours. Figure 7 shows the longitudinal and transversal creep displacement curves for all configurations. The DEM results closely match theoretical predictions, with a maximum relative difference of 2.6% for constant and linear loads and up to 4.2% for cyclic load.

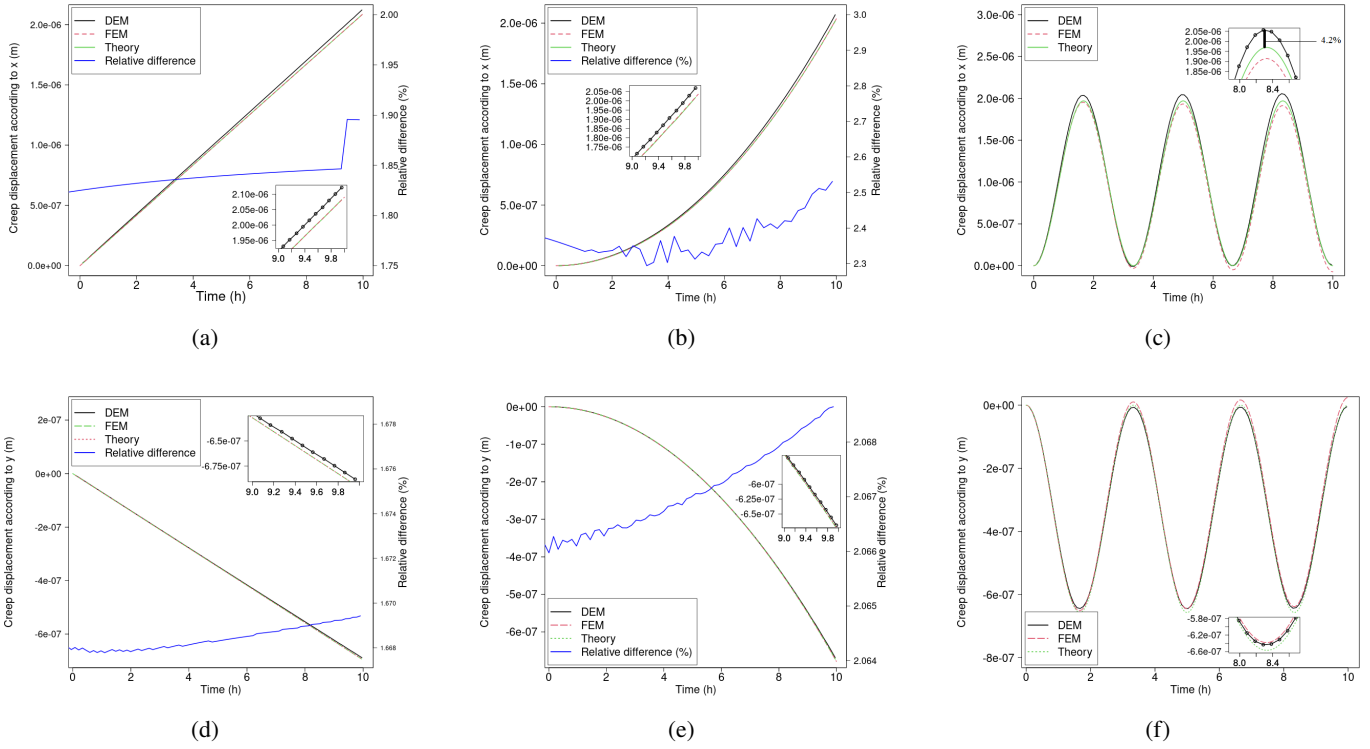


Fig. 7: Longitudinal and transversal creep displacements: (a)-(d): Constant load, (b)-(e): Linear load, (c)-(f): Cyclic load

By plotting the total Von-Mises (VMt) stress curve, derived by averaging σ_{VM} across all discrete elements (DEs), and comparing it with local Von-Mises stresses for DEs 1 to 6 (as detailed in Table 1 and Figure 6), we should note that the σ_{VMt} stress matches well the FEM Von-Mises stress. However, noticeable discrepancies are present at the DE level compared to FEM results. The largest relative difference is observed at the position of the DE1, with maximal relative differences of 28%, 19.1%, and 11.8% under constant, linear, and cyclic loads, respectively. These discrepancies can be attributed to the inherent variability of DEM, which is sensitive to changes in load conditions and can lead locally to significant variations in stress calculations (Moukadiri et al. (2019)). In the study led by Moukadiri et al. (2019), stress distribution was analysed through a specific tensile test for which the stress field is theoretically homogeneous. The Coefficient of Variation (CoV) was assessed to quantify the variation of local stress relative to the average one. Numerical tests revealed that the CoV can reach a value of 46.3% according to the density of particulate system and the definition of microscopic parameters. The use of smoothing techniques, such as the halo approach proposed by Moukadiri et al. (2019) contributes to reduce fluctuations in the stress field. This introduces a mesoscopic scale described by a circular geometry in 2D to each DE of the system. This geometry called halo allows for evaluating stress considering more neighbouring particles using Love-Weber formulation. Despite its relevance in smoothing the stress field, the halo approach is not used in the present study, because the latter requires a careful calibration protocol that takes into account the microscopic properties of the discrete model, otherwise it could generate a numerical bias at the DEs scale. Note that the largest difference is observed for DE1 which is located in the left edge, knowing that edge elements are more sensitive to stress variability. Despite these variations, the overall results for creep displacements and stresses highlight the suitability of the proposed DEM-based creep model in the case of tensile creep tests.

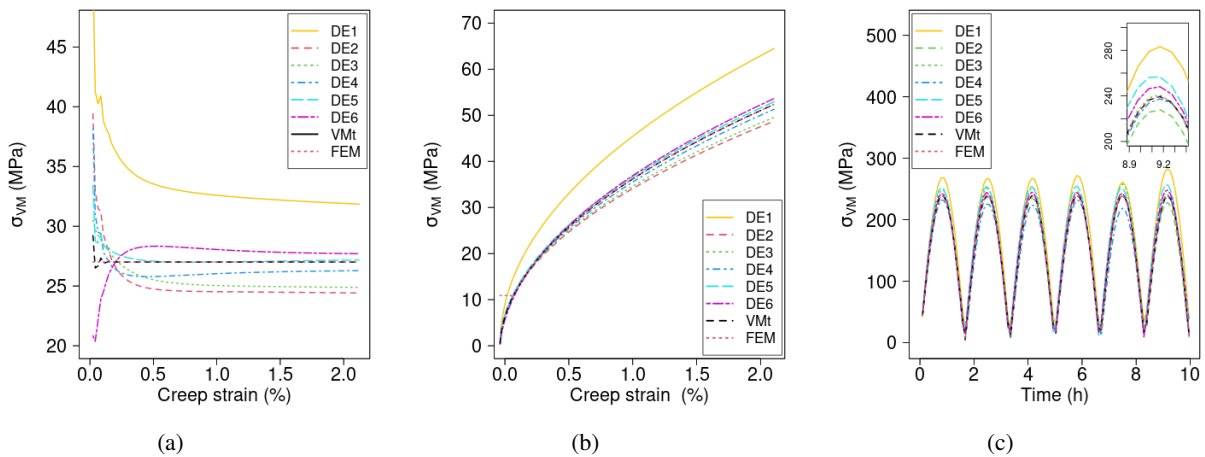
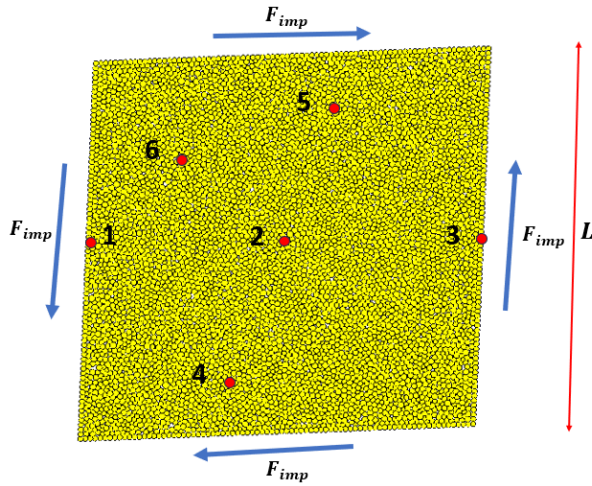


Fig. 8: Von-Mises stress vs creep strain: (a) Constant load, (b) Linear load, (c) Cyclic load

2.2.2 Shear test

Shear creep test is conducted on a 2D square sample with a length of $L = 10^{-5}m$ using a particulate system of 1000 DEs. A shear load, F_{imp} , is applied uniformly along every boundary, as illustrated in Figure 9. This test is carried out at a constant temperature

of 1100 °C on BC material for a duration of 10 hours. The applied load intensity is set to $2.5 \cdot 10^{-2}$ N, designed to achieve a strain of 2% by the end of the simulation, which corresponds to a time of $t = 10$ hours.



DEs	Coordinates (x,y)
1	(0L, 0.5L)
2	(0.5L, 0.5L)
3	(L, 0.5L)
4	(0.4L, 0.2L)
5	(0.6L, 0.8L)
6	(0.2L, 0.7L)

Fig. 9: Shear test configuration and applied boundary conditions

Tab. 3: Coordinates of DE 1 to 6

The shear creep displacement is compared with theoretical predictions, as shown in Figure 10 (a). The results indicate that the relative difference between the DEM and theoretical creep displacements is very small, not exceeding 1.4%, demonstrating a strong agreement between the DEM-based numerical and analytical results. Additionally, Von-Mises stress for DEs 1 to 6 in Figure 10 (b) agrees well with the expected theoretical value, except for DE3 which exhibits the maximum relative difference, approximately 25.4% at the end of the simulation ($t = 10h$). This difference observed in the shear test is attributed to the same factors as discussed in the context of tensile test. In particular, in DEM simulations, stresses at the edges are more variable due to the reduced number of neighbouring particles and unbalanced forces. These results show the validity of the DEM-based creep model in the context of the shear test.

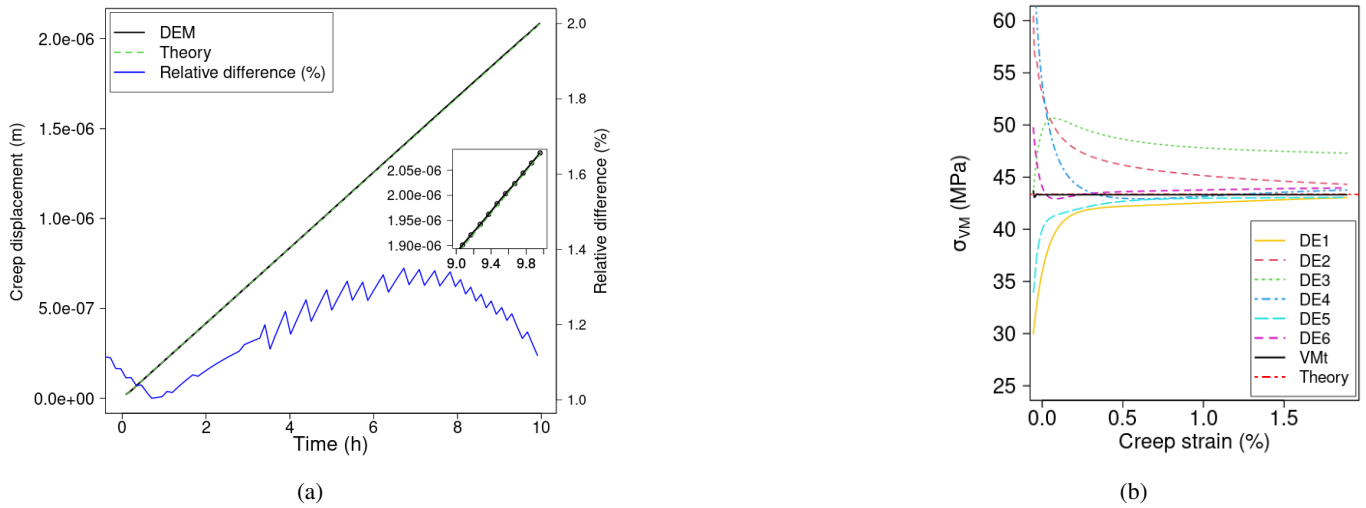


Fig. 10: (a) Shear creep displacement (b) Von-Mises stress evolution over the time

3 Application to a TBC microstructure

3.1 SEM image-based DEM modeling

The focus is set now to apply the DEM-based creep model to the case of a unit cell model of TBC as illustrated on Figure 11. A particulate system composed of 45 000 DE is handled based on the work of Ferguen et al. (2023), which takes into account BC, TC and TGO layers. Our model is extracted from a SEM image of TBC including the TGO layer growth as illustrated in Figures 11 (a) and (b). The length of domain is $L= 36 \mu\text{m}$ with a width $b=12 \mu\text{m}$. In this model, the interface between TC and BC is described using a sinusoidal profile, the wavelength and amplitude of which are set at 12 and 5 μm , respectively, according to the works of the literature (Cen et al. (2019); Rabiei and Evans (2000); Liu et al. (2016)). Note that symmetry boundary conditions are imposed on the bottom and right side surfaces of the model to represent only one half of the roughness (Bäker (2012); Cen et al. (2019)).

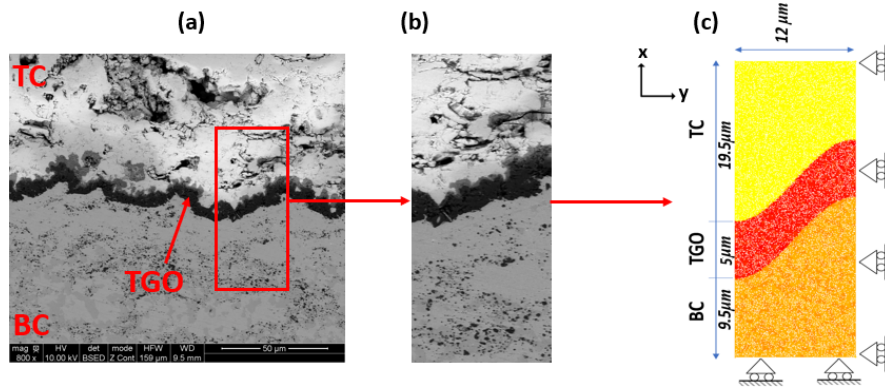


Fig. 11: TBC unit cell model. a) SEM image of a TBC microstructure obtained at 200 hours of holding time at 1100 °C , b) Extracted sample of interface roughness, c) DEM model with applied boundary conditions

All constitutive layers are assumed to be homogeneous and isotropic. Table 3 provides the temperature-dependent data for the CTE, Young's moduli and Poisson's ratios of all layers. Creep prefactor B and n exponent values are listed in Table 4, note that creep is only activated above 700 °C (Ranjbar-Far et al. (2010); Cen et al. (2019)). For the thermal history, the thermal cycle is illustrated in Figure 12 as discussed in subsection 1.3.

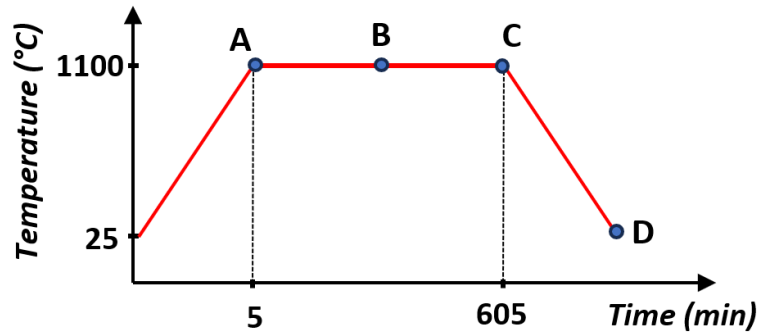


Fig. 12: Illustration of the thermal loading history with symbols A, B, C, and D designating the end of heating, midpoint of dwelling, end of dwelling, and end of cooling phases, respectively.

The oxide layer has an initial thickness of 5 μm and is bound to grow during thermal exposure due to the oxidation of the BC. In the present work, the TGO thickness, dependent on oxidation time, is determined based on experimental work in which TBC samples are placed in high-temperature furnace so that the interface oxidation of the TBC occurs and growth for various periods of time. Then the interface oxidation is analyzed by SEM characterization. Thus, the TGO layer thickness was measured using SEM images, leading to the formulation of the following TGO growth law (Liu et al. (2016)):

$$h = Kt^{0.5} \quad (9)$$

where K is the growth rate (0.3646 μm), h is the TGO thickness in μm and t is the dwelling time at high temperature (h). The growth occurs based on the predefined law set during the dwelling phase. The thickness of the TGO layer increases at the expense of the TC layer, so the DEs at the TGO/TC interface, which originally belonged to the TC layer, will now be located in the TGO layer.

Tab. 4: Temperature-dependent data for creep parameters B and n used for TC, BC and TGO layers (Ranjbar-Far et al. (2010); Bäker (2012); Cen et al. (2019))

	Temperature [°C]	B [$s^{-1}MPa^{-n}$]	n
TC	[700-1100]	$1.8 \cdot 10^{-8}$	1
TGO	[700-1100]	$7.3 \cdot 10^{-8}$	1
BC	[700-1100]	$1.11 \cdot 10^{-7}$	1

3.2 Results

3.2.1 Stress field

The stress field distributions are shown in Figure 13 (a) and (b) for point A at the end of the heating phase and point D at the end of the cycle respectively. Stresses at the TGO/BC interface are significant due to the CTE mismatch during the heating phase (Point A). At this point, the σ_{xx} stress field shows a minimum compressive stress of 181 MPa at the peak region of the BC/TGO interface and a maximum tensile stress of 234 MPa, at the valley region, as illustrated in the Figure 13 (a). Figure 13 (b) also presents a

contour plot of σ_{xx} stresses in TBC system at the end of the thermal cycle. Due to the CTE mismatch and creep effect, an inversion of stress locations is observed. Significant tensile stresses are present in the BC at the peak regions, with the maximum value reaching up to 681 MPa at the end of the cycle, corresponding to residual stress.

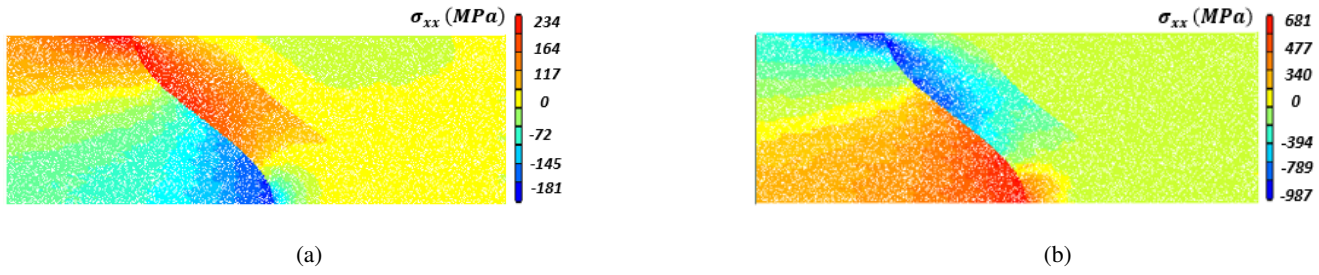


Fig. 13: σ_{xx} stress field distribution : (a) at point A (end of heating phase) (b) at point D (end of the cycle)

3.2.2 Time evolution of local stress

Time evolution of local σ_{xx} values during the heating up phase for both DEM and FEM simulations are presented in Figure 15 (a) and (b). These curves correspond to points DE1 and DE2 respectively, which are located at the peak (compression) and valley (tensile) regions of the BC/TGO interface respectively, as specified by their coordinates in Table 5.

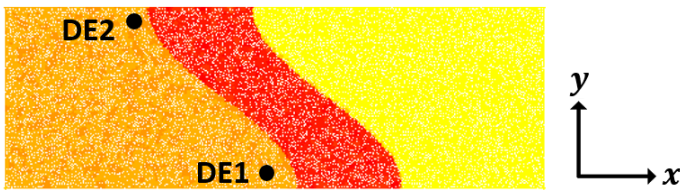
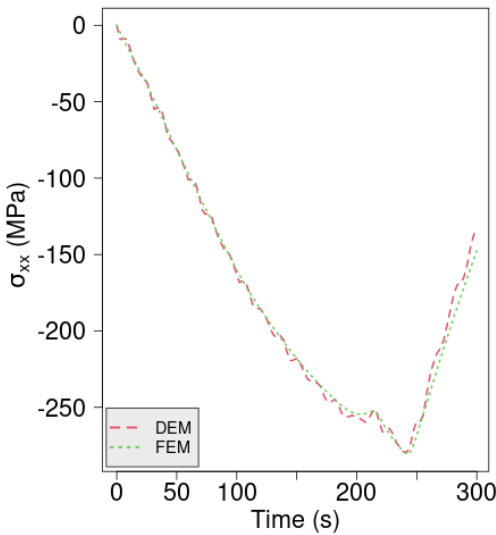


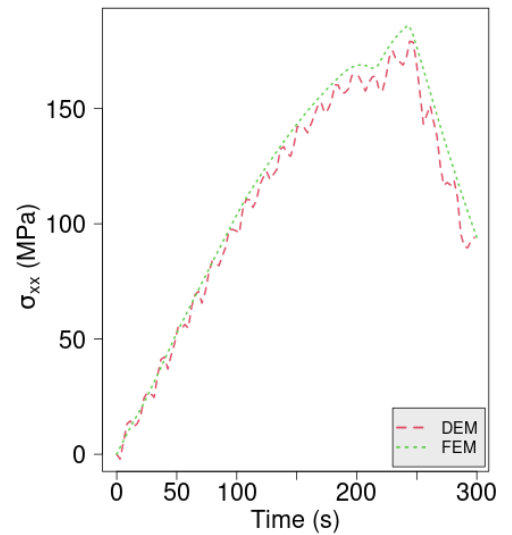
Fig. 14: Illustration of the location of DE 1 and 2

DEs	Coordinates (x,y)
1	(0.5L, 0.1b)
2	(0.25L, 0.85b)

Tab. 5: Coordinates of DE 1 and 2



(a) σ_{xx} at DE1

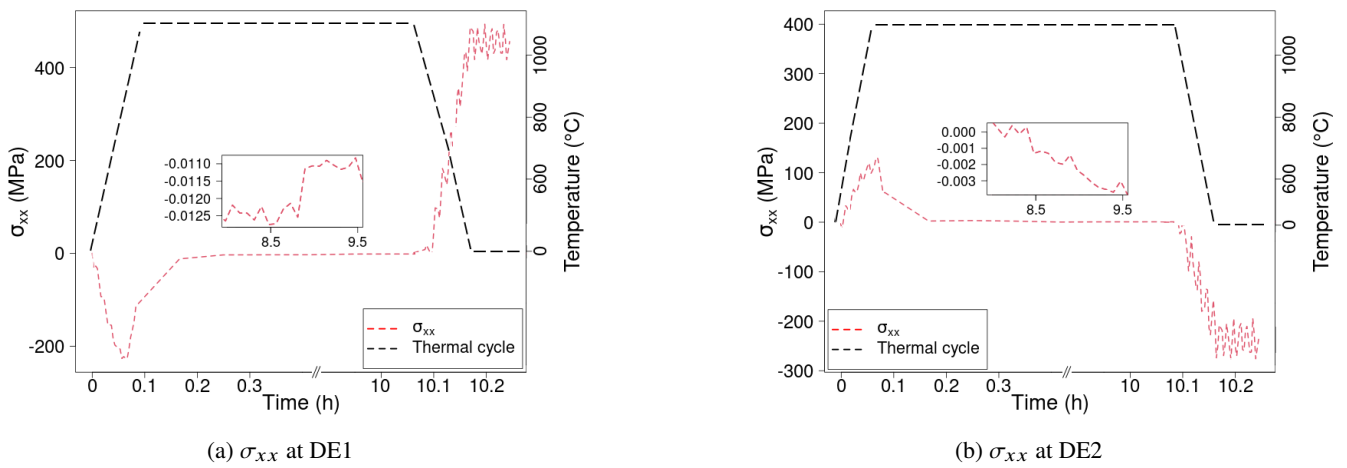


(b) σ_{xx} at DE2

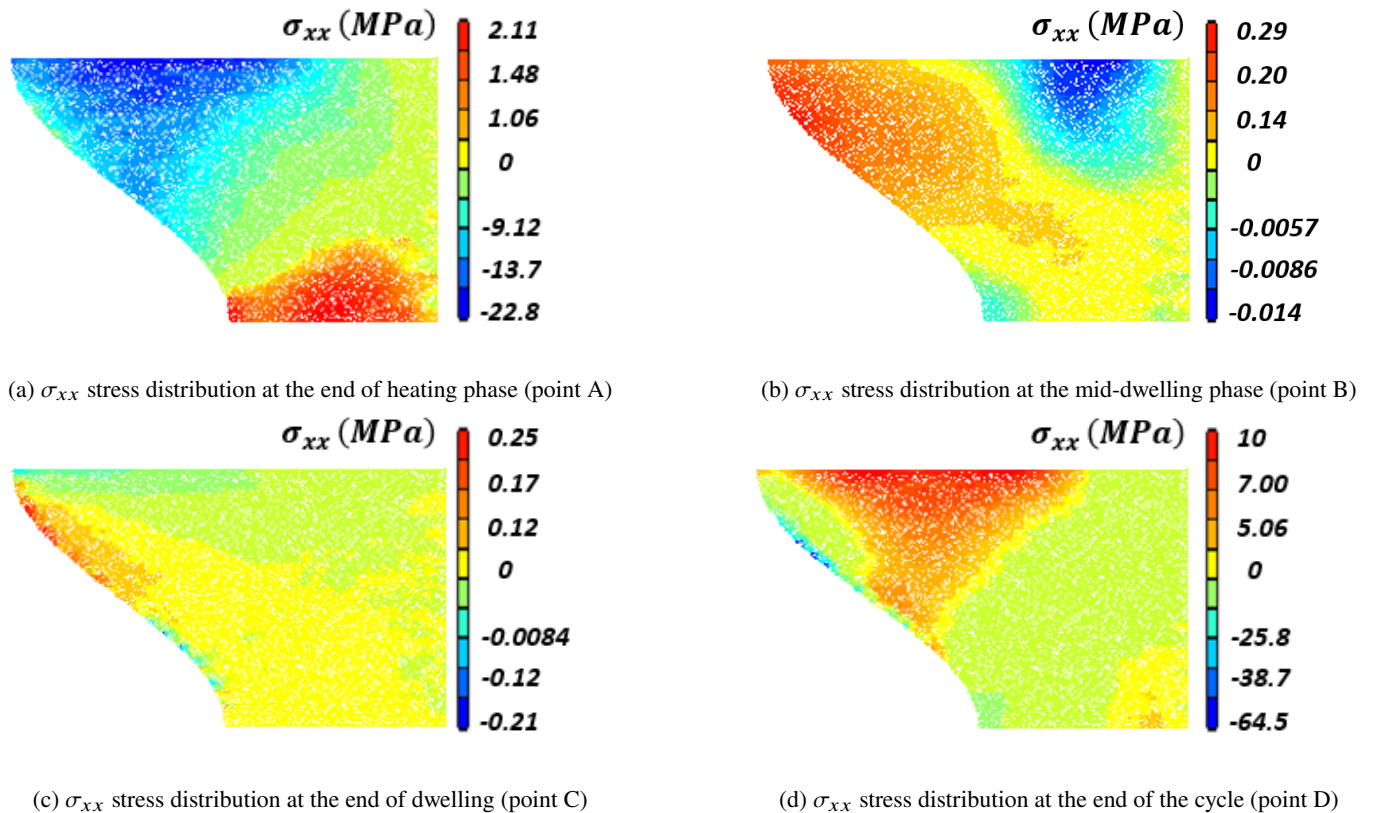
Fig. 15: Time evolution of local σ_{xx} during the heating phase

Locally, there is a good agreement between DEM and FEM results. The maximum relative difference for σ_{xx} is approximately 4.2%. It is important to note that stress reduction occurs when creep is activated at 700 °C, as indicated in Table 4, which corresponds to a heating time of roughly 200 seconds. Local results show strong correlation between FEM and DEM that were conducted under same conditions.

To further explore creep effects, time evolution of local σ_{xx} at points DE1 and DE2 are plotted in Figures 16 (a) and (b). During thermal exposure, creep significantly reduces the stresses, bringing the maximum tensile stress down to about 0.02 MPa at the end of dwelling phase as seen in the curves in Figures 16 (a) and (b). Upon cooling to ambient temperature, σ_{xx} stresses values increase again due to CTE mismatch.

Fig. 16: Time evolution of local σ_{xx} during the thermal cycle

3.2.3 Stress field in the TC

Fig. 17: σ_{xx} stress distribution at the 4 time points in the TC layer

Figures 17 (a), (b), (c) and (d) illustrate the distribution of σ_{xx} in the TC at four distinct time points of the thermal cycle (Figure 12). These stresses are concentrated near the TC/TGO interface. At high temperatures, the CTE mismatch induces tensile stresses in the peak region and compressive ones at the valley regions. At the peak region inside the TC, tensile stresses can reach up to 2.11 MPa. At elevated temperatures, the stresses at the valley regions shift from compressive to tensile, while those in the peak regions shift from tensile to compressive. Seiler et al. (2012) and Pature et al. (2002) have reported that stress reversal occur in the TC layer during thermal cycling at high temperature as the TGO thickens. Thus, stress conversion is linked to both CTE mismatch and the TGO growth. Additionally, significant stress relief occurs during thermal exposure due to creep, with maximum tensile stresses dropping to about 0.29 MPa at time point B. This reversal in the stress distribution in the TC undulation valley from compression to tension leads to cracking in the TC at the "valleys" between the peaks (mechanism IV in Figure 2).

4 Conclusions and perspectives

DEM-based approach has been developed to simulate the creep behavior of a TBC and the TGO growth during a thermal cycle. In first step, tensile and shear validation tests were performed on a homogeneous material at high temperature ($T=1100\text{ }^{\circ}\text{C}$). The

comparison between DEM, FEM and theoretical creep displacement and σ_{VM} stress exhibited a quite good agreement. In a second step, the DEM-based approach was applied to simulate the thermo-mechanical behavior of a TBC during a thermal cycle using a numerical model based on a sinusoidal interface profile taking into account TGO growth at high temperature, thermal expansion and visco-elastic creep effects. The study focused on analyzing stresses at the TGO/TC and BC/TGO interfaces. As expected, we observed that when creep is taking place, stress levels for σ_{xx} is reduced. Furthermore, results obtained from both DEM and FEM simulations displayed a good agreement in terms of creep displacement and stress values during the heating phase. Stress conversion in the TC layer occurs at high temperatures due to isothermal oxidation. In a next future, we aim to simulate interfacial debonding of TBC modeled using a real SEM image.

References

- J. Aktaa, K. Sfar, and D. Munz. Assessment of tbc systems failure mechanisms using a fracture mechanics approach. *Acta materialia*, 53(16):4399–4413, 2005. doi: [10.1016/j.actamat.2005.06.003](https://doi.org/10.1016/j.actamat.2005.06.003).
- G. Alhajj-Hassan, W. Leclerc, C. Pélegris, M. Guessasma, and E. Bellenger. On the suitability of a 3D discrete element method to model the composite damage induced by thermal expansion mismatch. *Computational Particle Mechanics*, 7(4):679–698, 2020. doi: [10.1016/j.ijthermalsci.2020.106799](https://doi.org/10.1016/j.ijthermalsci.2020.106799).
- A. Ammar, W. Leclerc, M. Guessasma, and N. Haddar. Discrete element approach to simulate debonding process in 3D short glass fibre composite materials : Application to PA6/GF30. *Composite Structures*, 270:114035, 2021. doi: [10.1016/j.compstruct.2021.114035](https://doi.org/10.1016/j.compstruct.2021.114035).
- D. André, I. Iordanoff, J. Charles, and J. Néauport. Discrete element method to simulate continuous material by using the cohesive beam model. *Computer methods in applied mechanics and engineering*, 213:113–125, 2012. doi: [10.1016/j.cma.2011.12.002](https://doi.org/10.1016/j.cma.2011.12.002).
- D. André, M. Jebahi, I. Iordanoff, J-L. Charles, and J. Néauport. Using the discrete element method to simulate brittle fracture in the indentation of a silica glass with a blunt indenter. *Computer Methods in Applied Mechanics and Engineering*, 265:136–147, 2013. doi: [10.1016/j.cma.2013.06.008](https://doi.org/10.1016/j.cma.2013.06.008).
- M. Bäker. Finite element simulation of interface cracks in thermal barrier coatings. *Computational Materials Science*, 64:79–83, 2012. doi: [10.1016/j.commatsci.2012.02.044](https://doi.org/10.1016/j.commatsci.2012.02.044).
- L. Cen, W-Y. Qin, and Q-M. Yu. Analysis of interface delamination in thermal barrier coating system with axisymmetric structure based on corresponding normal and tangential stresses. *Surface and Coatings Technology*, 358:785–795, 2019. doi: [10.1016/j.surfcoat.2018.12.008](https://doi.org/10.1016/j.surfcoat.2018.12.008).
- P-A. Cundall. Rational design of tunnel supports: A computer model for rock mass behavior using interactive graphics for the input and output of geometrical data. Technical report, Minnesota University Minneapolis Department of Civil and Mining Engineering, 1974.
- N. Ferguen, W. Leclerc, and E-S. Lamini. Numerical investigation of thermal stresses induced interface delamination in plasma-sprayed thermal barrier coatings. *Surface and Coatings Technology*, page 129449, 2023. doi: [10.1016/j.surfcoat.2023.129449](https://doi.org/10.1016/j.surfcoat.2023.129449).
- A. Feuerstein, J. Knapp, T. Taylor, A. Ashary, A. Bolcavage, and N. Hitchman. Technical and economical aspects of current thermal barrier coating systems for gas turbine engines by thermal spray and ebpdv: a review. *Journal of Thermal Spray Technology*, 17(2):199–213, 2008. doi: [10.1007/s11666-007-9148-y](https://doi.org/10.1007/s11666-007-9148-y).
- H. Haddad, W. Leclerc, M. Guessasma, C. Pélegris, N. Ferguen, and E. Bellenger. Application of DEM to predict the elastic behavior of particulate composite materials. *Granular Matter*, 17(4):459–473, 2015. doi: [10.1007/s10035-015-0574-0](https://doi.org/10.1007/s10035-015-0574-0).
- H. Haddad, M. Guessasma, and J. Fortin. A dem–fem coupling based approach simulating thermomechanical behaviour of frictional bodies with interface layer. *International Journal of Solids and Structures*, 81:203–218, 2016. doi: [10.1016/j.ijsolstr.2015.11.026](https://doi.org/10.1016/j.ijsolstr.2015.11.026).
- T-H. Hyde, W. Sun, and C-J. Hyde. *Applied creep mechanics*. 2014.
- S. Ji, S. Wang, and Z. Peng. Influence of external pressure on granular flow in a cylindrical silo based on discrete element method. *Powder Technology*, 356:702–714, 2019. doi: [10.1016/j.powtec.2019.08.083](https://doi.org/10.1016/j.powtec.2019.08.083).
- S-T. Kyaw, I-A. Jones, and T-H. Hyde. Simulation of failure of air plasma sprayed thermal barrier coating due to interfacial and bulk cracks using surface-based cohesive interaction and extended finite element method. *The Journal of Strain Analysis for Engineering Design*, 51(2):132–143, 2016. doi: [10.1177/0309324715615746](https://doi.org/10.1177/0309324715615746).
- W. Leclerc. Discrete element method to simulate the elastic behavior of 3D heterogeneous continuous media. *International Journal of Solids and Structures*, 121:86–102, 2017. doi: [10.1016/j.ijsolstr.2017.05.018](https://doi.org/10.1016/j.ijsolstr.2017.05.018).
- W. Leclerc, H. Haddad, and M. Guessasma. On the suitability of a Discrete Element Method to simulate cracks initiation and propagation in heterogeneous media. *International Journal of Solids and Structures*, 108:98–114, 2017. doi: [10.1016/j.ijsolstr.2016.11.015](https://doi.org/10.1016/j.ijsolstr.2016.11.015).
- W. Leclerc, N. Ferguen, and E-S. Lamini. Discrete element method to simulate interface delamination and fracture of plasma-sprayed thermal barrier coatings. *Modelling and Simulation in Materials Science and Engineering*, 30(4):045012, 2022. doi: [10.1088/1361-651x/ac6438](https://doi.org/10.1088/1361-651x/ac6438).
- X. Liu, T. Wang, C. Li, Z. Zheng, and Q. Li. Microstructural evolution and growth kinetics of thermally grown oxides in plasma sprayed thermal barrier coatings. *Progress in Natural Science: Materials International*, 26(1):103–111, 2016. doi: [10.1016/j.pnsc.2016.01.004](https://doi.org/10.1016/j.pnsc.2016.01.004).

- D. Moukadiri, W. Leclerc, K. Khellil, Z. Aboura, M. Guessasma, and al. Halo approach to evaluate the stress distribution in 3d discrete element method simulation: Validation and application to flax/bio based epoxy composite. *Modelling and Simulation in Materials Science and Engineering*, 27(6):065005, 2019. doi: [10.1088/1361-651x/ab20d3](https://doi.org/10.1088/1361-651x/ab20d3).
- N. Padture, M. Gell, and E-H. Jordan. Thermal barrier coatings for gas-turbine engine applications. *Science*, 296(5566):280–284, 2002. doi: [10.1126/science.1068609](https://doi.org/10.1126/science.1068609).
- D. Potyondy and P-A. Cundall. A bonded-particle model for rock. *International journal of rock mechanics and mining sciences*, 41(8):1329–1364, 2004. doi: [10.1016/j.ijrmms.2004.09.011](https://doi.org/10.1016/j.ijrmms.2004.09.011).
- E-A. Rabiei and A-G. Evans. Failure mechanisms associated with the thermally grown oxide in plasma-sprayed thermal barrier coatings. *Acta materialia*, 48(15):3963–3976, 2000. doi: [10.1016/s1359-6454\(00\)00171-3](https://doi.org/10.1016/s1359-6454(00)00171-3).
- M. Ranjbar-Far, J. Absi, G. Mariaux, and F. Dubois. Simulation of the effect of material properties and interface roughness on the stress distribution in thermal barrier coatings using finite element method. *Materials & Design*, 31(2):772–781, 2010. doi: [10.1016/j.matdes.2009.08.005](https://doi.org/10.1016/j.matdes.2009.08.005).
- P. Seiler, M. Bäker, and J. Rösler. Influence of creep and cyclic oxidation in thermal barrier coatings. *International journal of materials research*, 103(1):50–56, 2012. doi: [10.3139/146.110629](https://doi.org/10.3139/146.110629).
- S. Torquato, T. Truskett, and P-G. Debenedetti. Is random close packing of spheres well defined? *Physical review letters*, 84(10):2064, 2000. doi: [10.1103/physrevlett.84.2064](https://doi.org/10.1103/physrevlett.84.2064).
- M. Zhou. A new look at the atomic level virial stress: on continuum-molecular system equivalence. *Proceedings of the Royal Society of London. Series A: Mathematical, Physical and Engineering Sciences*, 459(2037):2347–2392, 2003. doi: [10.1098/rspa.2003.1127](https://doi.org/10.1098/rspa.2003.1127).